A High-Speed Hyperspectral Laparoscopic Imaging System

Kelden Pruitt [a,b], Brett Johnson[c], Jeffrey Gahan[c], Ling Ma [a,b], Baowei Fei [a,b,d *]

[a] Department of Bioengineering, University of Texas at Dallas, Richardson, TX
[b] Center for Imaging and Surgical Innovation, University of Texas at Dallas, Richardson, TX
[c] University of Texas Southwestern Medical Center, Department of Urology, Dallas, TX
[d] University of Texas Southwestern Medical Center, Department of Radiology, Dallas, TX

* Corresponding author: bfei@utdallas.edu, Website: https://fei-lab.org

ABSTRACT

Minimally invasive surgery (MIS) has expanded broadly in the field of abdominal and pelvic surgery. Laparoscopic and robotic surgery has improved surgeon ergonomics, instrument precision, operative time, and postoperative recovery across various abdominal procedures. The goal of this study is to establish the feasibility of implementing high-speed hyperspectral imaging into a standard laparoscopic setup and exploring its benefit to common intracorporeal procedures. A hyperspectral laparoscopic imaging system was constructed using a customized hyperspectral camera alongside a standard rigid laparoscope and was validated for both spectral and spatial accuracy. Demosaicing methods were investigated for improved full-resolution visualization. Hyperspectral cameras with different spectral ranges were considered and compared with one another alongside two different light sources to determine the most effective configuration. Finally, different porcine tissues were imaged *ex-vivo* to test the capabilities of the system and spectral footprints of the various tissues were extracted. The tissue was also imaged in a phantom to simulate the system's use in MIS. The results demonstrated a hyperspectral laparoscopic imaging system that could provide quantitative, diagnostic information while not disrupting normal workflow nor adding excessive weight to the laparoscopic setup. The high-speed hyperspectral laparoscopic imaging system can have immediate applications in image-guided surgery.

Keywords: Hyperspectral imaging, minimally invasive surgery, robotic surgery, image-guided intervention

1. INTRODUCTION

Laparoscopic and robotic surgery have been increasing in prevalence across all surgical specialties for decades, including urology. Along with the prevalence of colorectal cancer, prostate cancer is the second most frequent cancer diagnosis made in men and the fifth leading cause of death worldwide [1]. While some cases remain indolent, others require surgical intervention to improve patient prognosis, a procedure that is commonly done laparoscopically. Along with the development of minimally invasive surgical procedures and techniques, the hardware and imaging systems that allow such procedures have been developed, refined, and improved upon as well. However, there are still prevalent issues surrounding intracorporeal surgery. In addressing adverse outcomes, such as anastomotic leakage and positive tumor margins, fluorescence imaging with indocyanine green (ICG), 3D stereoscopic visualization, and narrow-band imaging have all been developed and incorporated in current state-of-the-art systems. But these still have drawbacks, such as the quick half-life of ICG or the lack of objective, quantitative analysis in real time [2, 3].

Hyperspectral imaging (HSI) is an emerging optical imaging modality that takes advantage of spectral characteristics of differing tissues. HSI has been investigated for its non-invasive, contrast-free, and quantitative applications such as tissue classification [4] and blood-oxygen saturation [5]. HSI has also seen use in disease diagnosis, histopathology, and surgical guidance [6], but a major drawback of current systems when implemented into a MIS application is long acquisition speeds which are usually on the order of seconds as well as bulky systems that are unable to translate into a feasible operative workflow. Kohler et. al. [7, 8] developed a hyperspectral system for laparoscopic imaging with similar accuracy to a commercially available system, but an HSI acquisition time of 4.6 seconds. On the other hand, Ayala et. al. [9] constructed a similar HSI system to the one presented but provided little information on spectral accuracy and spatial resolution. As such we will address, expand upon and apply this setup to different spectral ranges.

The field of laparoscopic imaging has evolved much through the efforts of various research groups in many areas, leading to advanced state-of-the-art systems including augmented/mixed reality capable systems [10-23], which further subdivides

Medical Imaging 2023: Image-Guided Procedures, Robotic Interventions, and Modeling, edited by
Cristian A. Linte, Jeffrey H. Siewerdsen, Proc. of SPIE Vol. 12466, 1246608
 · 1605-7422 · doi: 10.1117/12.2653922

into hyperspectral imaging (HSI) systems [24-35] and combinatory operative imaging systems [36-38], dual/multi modal systems [39-43], and high speed hyperspectral systems [44]. Each system seeks to improve the current capabilities of surgical imaging in laparoscopic procedures by providing additional diagnostic data as well as methods for interpreting that data. This work aims to show the feasibility and application of newly developed high-speed hyperspectral technology in a laparoscopic imaging workflow. Our system is distinctly different from most hyperspectral systems in the underlying technology and is coupled with demosaicking techniques to provide spectral information quickly and not fully compromise the spatial resolution of the imager.

2. METHODS

Our hyperspectral imaging system is constructed to simulate intracorporeal laparoscopic visualization. Technical validations are performed to assess the capabilities of the hyperspectral imaging technology in both the spatial and spectral dimension. Finally, *ex vivo* tissue images were acquired on porcine visceral tissues including stomach, intestine, liver, and kidney tissue samples, including images taken within an abdominal model.

2.1 Imaging Setup

Figure 1 shows our hyperspectral laparoscopic imaging setup that included a 10 mm, 0° laparoscope (UHD IR Telescope, Olympus America | Medical) along with a 300W xenon light source (Visera Elite II Xenon IR, Olympus America | Medical), C-mount adapter, and a customized hyperspectral camera capable of capturing up to 120 hypercubes/sec through the use of mosaic filters in either 4x4 or 5x5 configurations. The spectral range of the visible (VIS) camera includes 16 wavelengths from 460-600 nm. The red/near-infrared (RNIR) camera includes 15 reflectance values at different wavelengths in the range of 600-870 nm. Lastly, the near-infrared (NIR) camera includes reflectance measurements at 24 wavelengths within the range of 660-960 nm. In order to utilize cameras extending into the near-infrared range, a halogen source (OSL2 High-Intensity Fiber-Coupled Illuminator, Thorlabs, Newton, NJ) was also included. The spectral range of the halogen source is 450-900 nm, covering the spectral range of the RNIR hyperspectral camera.

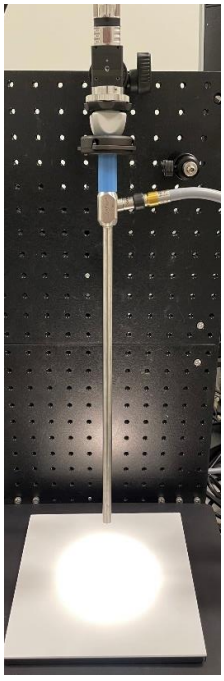

Figure 1. Hyperspectral laparoscopic imaging setup with white reference tile.

2.2 Data Processing

Data processing was performed in MATLAB (MathWorks Inc, Natick, MA, USA) and included hypercube reconstruction, demosaicing, and spectral analysis. Hypercube reconstruction was necessary to analyze the hypercubes of raw mosaic imaging files and compared against processed hypercubes derived from the software used to capture images as well as calculate band-wise sums for the band averaging demosaicing technique. Multiple demosaicing algorithms were considered, the simplest being the normalization from an image of the white reference. Other algorithms included the band averaging technique and low-pass filtering technique performed on the raw mosaic image. These demosaicing algorithms provided full resolution images to evaluate the spatial resolution. To analyze the tissue spectra derived from the hyperspectral cameras, a binary mask of the tissue was generated semi-automatically. Hyperspectral images were calibrated to a white reference according to Equation (1), where the used standard is 95% reflectance white reference:

$$I_{\text{reflectance}}(\lambda) = \frac{I_{\text{processed}}(\lambda)}{I_{\text{WR}}(\lambda)} \quad (1)$$

where $I_{\text{reflectance}}$ is the calibrated reflectance intensity, $I_{\text{processed}}$ and I_{WR} is the dark-reference corrected reflectance intensity of the tissue and white reference, respectively. Dark-reference correction accounts for the dark current of the camera, which is found by subtracting the dark current image intensities from the actual image intensities. Calibrated reflectance values were then acquired over the tissue masks in each hyperspectral image to produce spectral footprints of the reflectance values at each wavelength of the imaged tissues. We also implemented a curvature correction processing technique that addresses the differences in reflectance intensity that results from curvature in the tissue and elevation of different areas of a specimen. This is particularly useful when imaging tissues with morphological features that alter the distance to the imager, such as bumps and elevations, or features that alter the incidence angle of the incoming light. When these features are present, it is assumed that spectra measured at two different points on the tissue could result in curves that follow the same footprint, but vary by some constant. The curvature correction technique allows for direct comparison of spectral shape irrespective of intensity. It's implemented by dividing each reflectance intensity at a pixel by the sum of all reflectance intensities over all wavelengths at the same pixel.

2.3 Spectral and Spatial Validation

To validate the spectral accuracy of the hyperspectral cameras, standard reflectance tiles were used (Spectralon, Labsphere, Inc., North Sutton, New Hampshire) to compare spectral footprints from hyperspectral images with standard reflectance curves provided from calibration files, which provide accurate reflectance values. The cut-on wavelength of the calibration curves is 360 nm and the cutoff wavelength is 830 nm, providing coverage for most of the spectral range of the hyperspectral cameras. For spectral validation, spectral curves were captured with the RNIR hyperspectral camera. Considering the spatial resolution capabilities of the setup, 1951 USAF Resolution Test Targets (Thorlabs, Newton, NJ) were imaged at working distances typical of laparoscopic procedures, 7 cm and 10 cm. These images were coupled with one of the proposed demosaicing techniques in order to take advantage of the full sensor resolution of the camera.

2.4 Evaluation of Image Quality

In order to measure spatial contrast, a Michelson contrast cutoff of 20% was used as shown in Equation (2) [45]:

$$\text{Contrast} = \frac{S_{max} - S_{min}}{S_{max} + S_{min}} \quad (2)$$

A perception-based image quality evaluator (PIQE) was used to evaluate the overall quality of the demosaicing techniques. This is an unsupervised and opinion-unaware no-reference algorithm that estimates distortion and local variance. A lower PIQE score indicates a higher quality image. For comparable results, the images from each of the demosaicing techniques were normalized to intensity values in the range of [0, 1], and each was brought to a similar brightness level qualitatively, as image brightness has an effect on PIQE scores.

2.5 Phantom Imaging Simulation

To further simulate intracorporeal procedures, abdominal tissues were placed in a phantom model and imaging was conducted, as seen in Figure 2. In this procedure, a porcine liver and two kidneys were put into the model for imaging. This allowed the exploration of the mobility and maneuverability of the system in a dynamic setting, which is opposed to the static setting for controlled imaging and testing. Our phantom consisted of a standard hollow mannequin that we altered

for the housing of *ex vivo* tissues. We then bored a 0.5" (1.27cm) hole in the abdomen below the umbilicus for the insertion of the 10 mm scope.

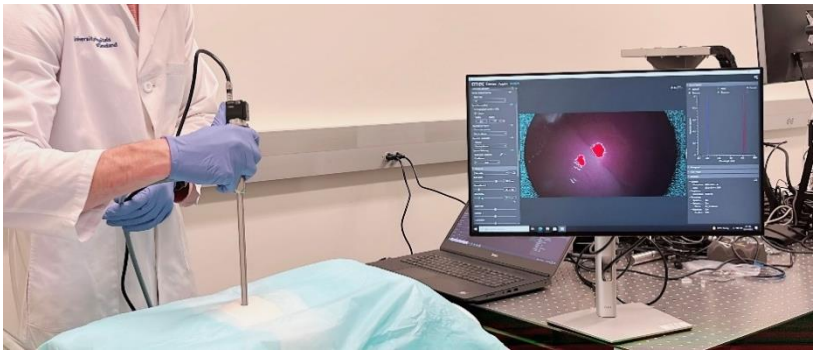

Figure 2. Laparoscopic imaging experiments in abdominal phantom. Laparoscopic view of porcine liver and kidney tissue interface, viewed as a pseudo-RGB image from the hypercube data.

2.6 *Ex-Vivo* Tissue Imaging

A porcine model was used for ex vivo tissue imaging including stomach, liver, kidney, and intestinal tissues. Tissues were resected and imaged in different areas to compare spectral characteristics under halogen illumination. The RNIR snapshot camera was used to image the tissue. Tissues were imaged for 30-40 frames each, resulting in 30-40 hypercubes per tissue. The system was capable of capturing 30 hypercubes in ~2 s with the selected imaging parameters. Mosaic images and hypercubes of each tissue were then averaged to reduce the effect of noise on each image and the corresponding spectra. Two images of each tissue were captured individually followed by an image with each tissue type in the field of view. A standard working distance of ~7cm was used and kept constant throughout the imaging experiments.

3. RESULTS

3.1 Spectral Validation Result on Reference Color Tiles

Spectral validation was performed on eight reference tiles (Figure 3). Spectral footprints of each tile were well represented in the spectral range of the RNIR camera, providing clear color distinction capabilities (Figure 4). Recorded reflectance values for the red and yellow reflectance standards were slightly greater than the reference reflectance values, but each curve still followed the overall trend of the standard tile. This shows that different spectral signatures can be distinguished by the camera and affirms the overall spectral accuracy of the system.

Figure 3. Spectralon reflectance tiles for the evaluation of the hyperspectral laparoscope system.

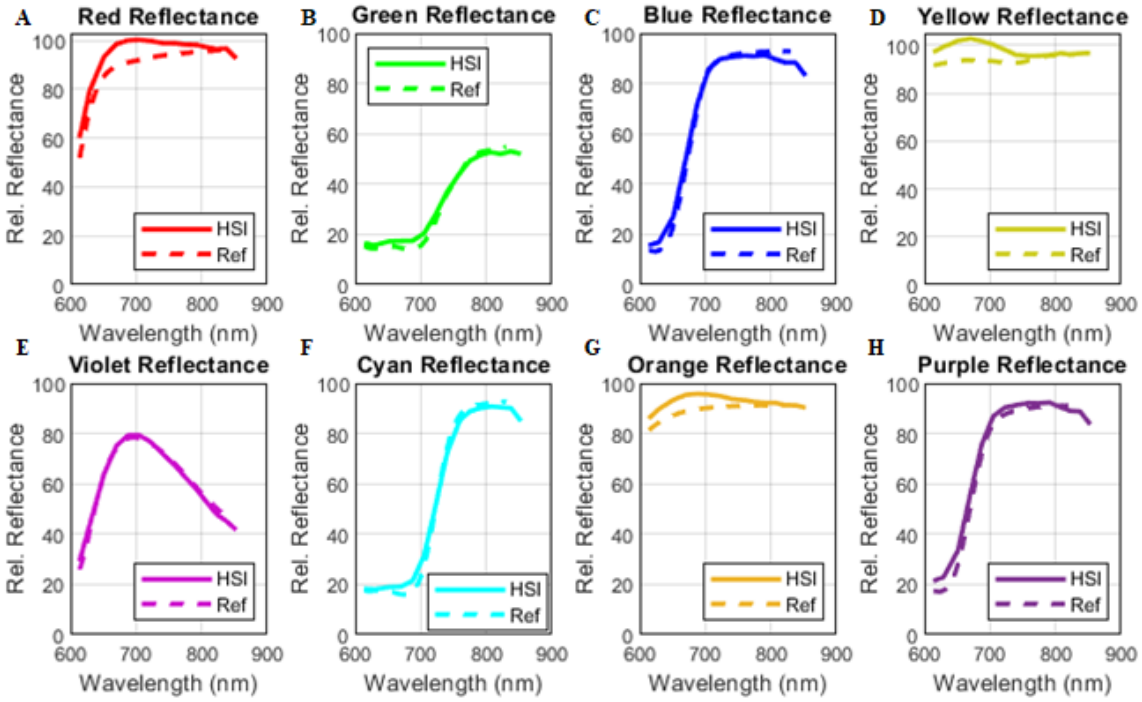

Figure 4. Results of spectral accuracy of RNIR camera (solid) against the tile standard reflectance (dashed). A) Red reflectance tile. B) Green reflectance tile. C) Blue reflectance tile. D) Yellow reflectance tile. E) Violet reflectance tile. F) Cyan reflectance tile. G) Orange reflectance tile. H) Purple reflectance tile.

3.2 Demosaicing Results

After performing the band-average demosaic technique, spatial validation originally resulted in an equal vertical and horizontal resolution of 1 mm for a 10 cm working distance. At 7 cm, an improvement to the horizontal resolution was seen of 0.8 mm. But, as significant sensor area was unused by the laparoscopic setup, a 2x video extender lens was included in the system. Further imaging at a working distance of 7 cm showed an improvement to sub-millimeter spatial resolution in the vertical and horizontal directions.

Each of the demosaicing techniques were applied at the same working distance for comparison. At 0.56 mm horizontal resolution, the low-pass filtering technique produced the highest Michelson contrast value of 21.9%, followed by the band-averaged image at 19.4% and lastly the white-reference calibrated image at 19.0%. At 0.56mm vertical resolution, each of the low-pass filtering and white reference calibration techniques were over the 20% threshold, while the band averaging technique had a vertical resolution of 0.63mm. According to the PIQE metric, band-average technique produced the highest quality image, as shown in Table 1. This confirms the qualitative conclusion when comparing the images, as the band-average demosaic image retains a slightly higher degree of sharpness. Each of the produced images can be seen in Figure 5.

3.3 *Ex-Vivo* Tissue Spectra

Tissue imaging was carried out using the RNIR camera, providing spectral reflectance from both long-wave visible and short-wave near-infrared (NIR) regions of light, to explore the significance of both regions of light. Blood absorption coefficients also vary distinctly in this RNIR region, providing clearer tissue distinctions and estimation of blood content [46]. Tissues were imaged individually and collectively, then hypercubes were attained through MATLAB processing and tissue masks were created for each specimen. Manual glare removal was performed prior to extracting the spectrum of each tissue. The resulting plot shows the mean reflectance values of each tissue, including their standard deviation (SD)

as shaded area above and below the curve, as seen in Figure 6. Each hyperspectral image and resulting individual tissue spectra are shown in Figures 7-10. Significant bands for tissue distinction are in the long-wave visible and NIR region of light. Higher variance in spectral reflectance is seen in intestinal and stomach tissues than liver and kidney tissues. Liver and kidney tissues overall are seen to have lower reflectance values, owing to their higher blood content relative to the other tissues, which leads to greater light absorption in the RNIR range. The produced images can be found as supplemental figures.

Table 1. PIQE scores for each demosaicing technique.

Technique	PIQE Score
Raw Mosaic	67.8
White Reference Calibration	22.9
Low-Pass Filter	27.8
Band Average	22.8

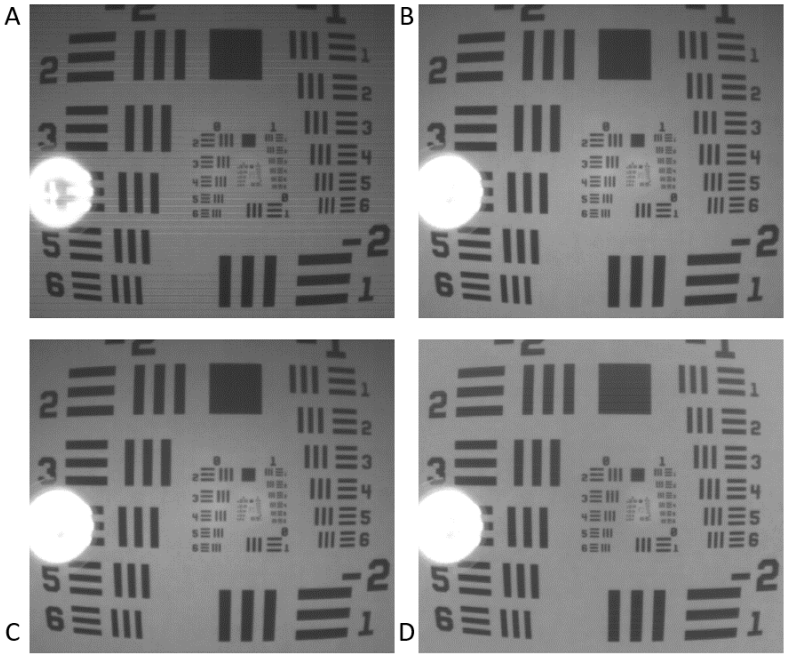

Figure 5. Images from three demosaicing methods. A) Original mosaic image. B) Low-pass filtering. C) Band-averaging. D) White reference calibration.

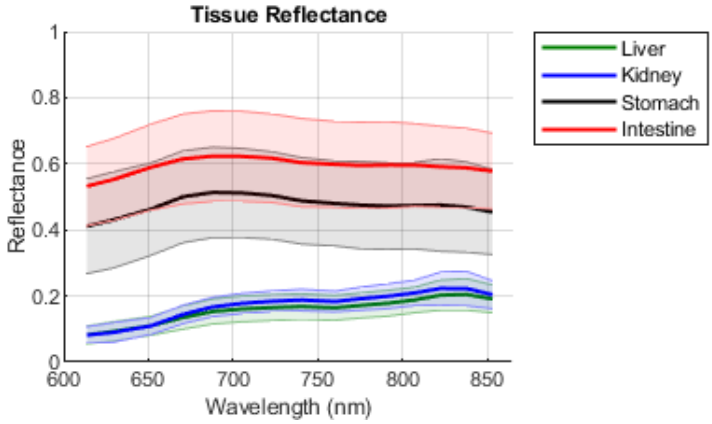

Figure 6. Mean reflectance of liver, kidney, stomach, and intestinal tissue plotted (± SD) against wavelength.

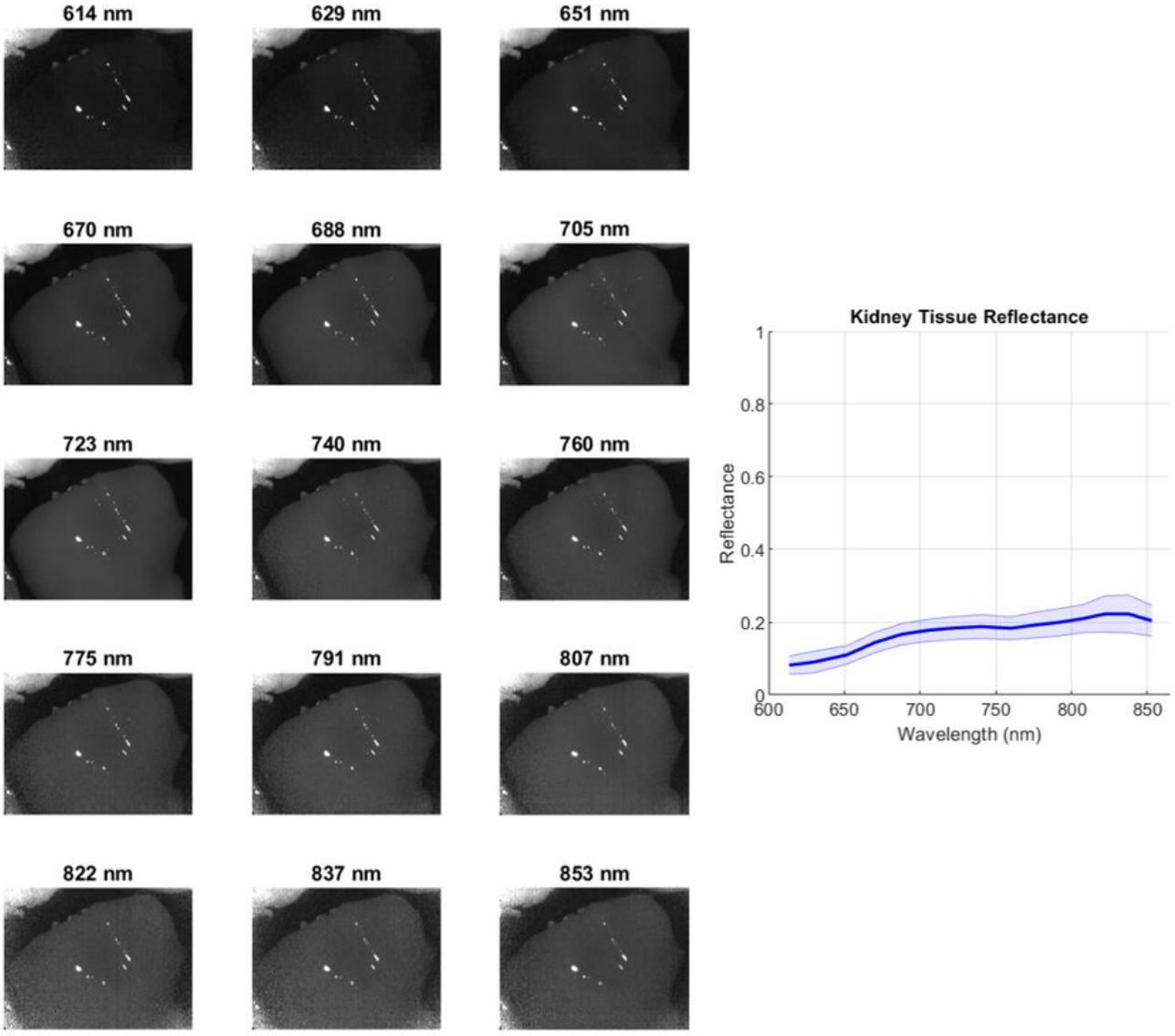

Figure 7. Hyperspectral image of porcine kidney tissue. Each band image is shown on the left, with the respective spectral curve on the right.

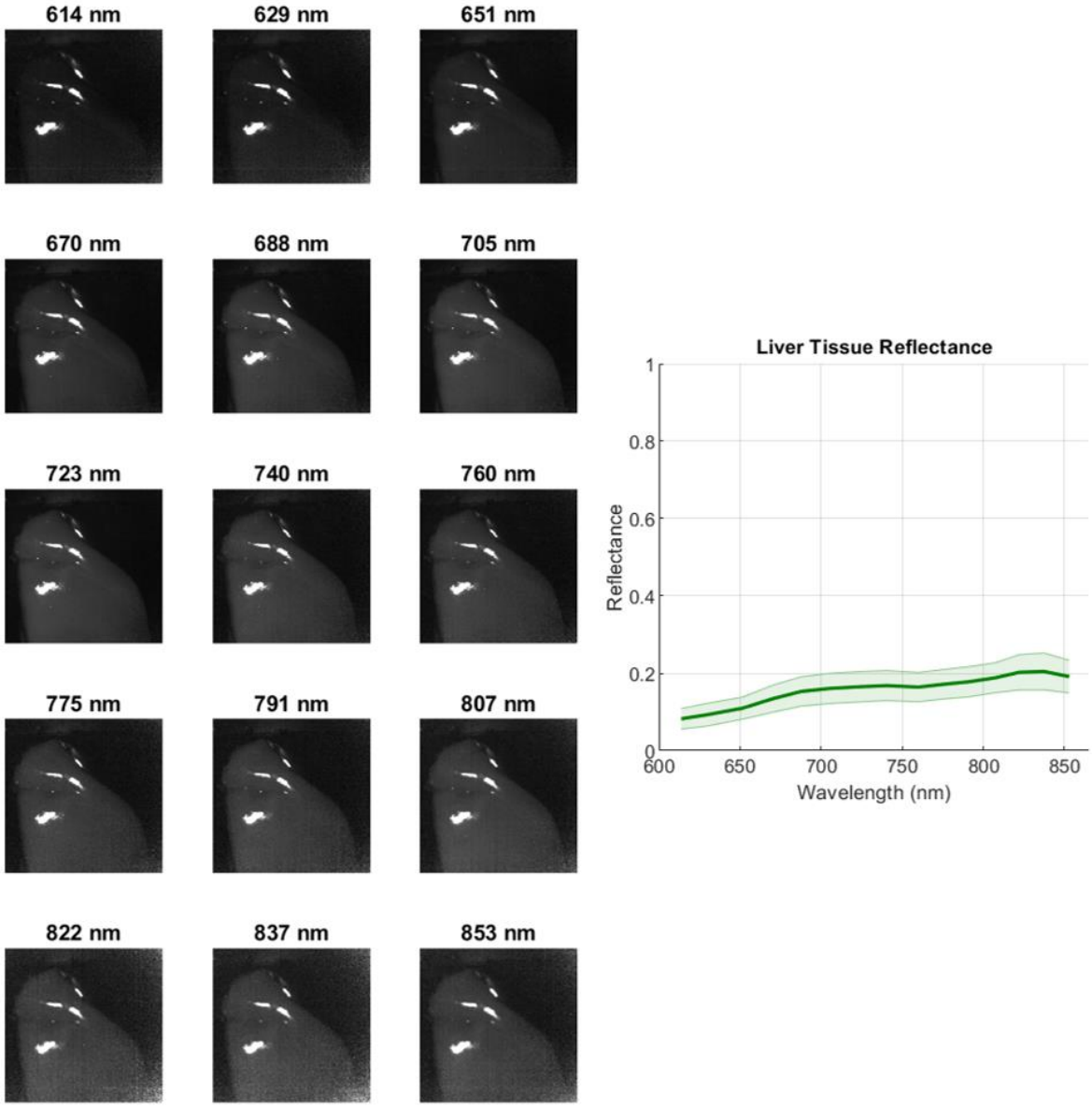

Figure 8. Hyperspectral image of porcine liver tissue. Each band image is shown on the left, with the respective spectral curve on the right.

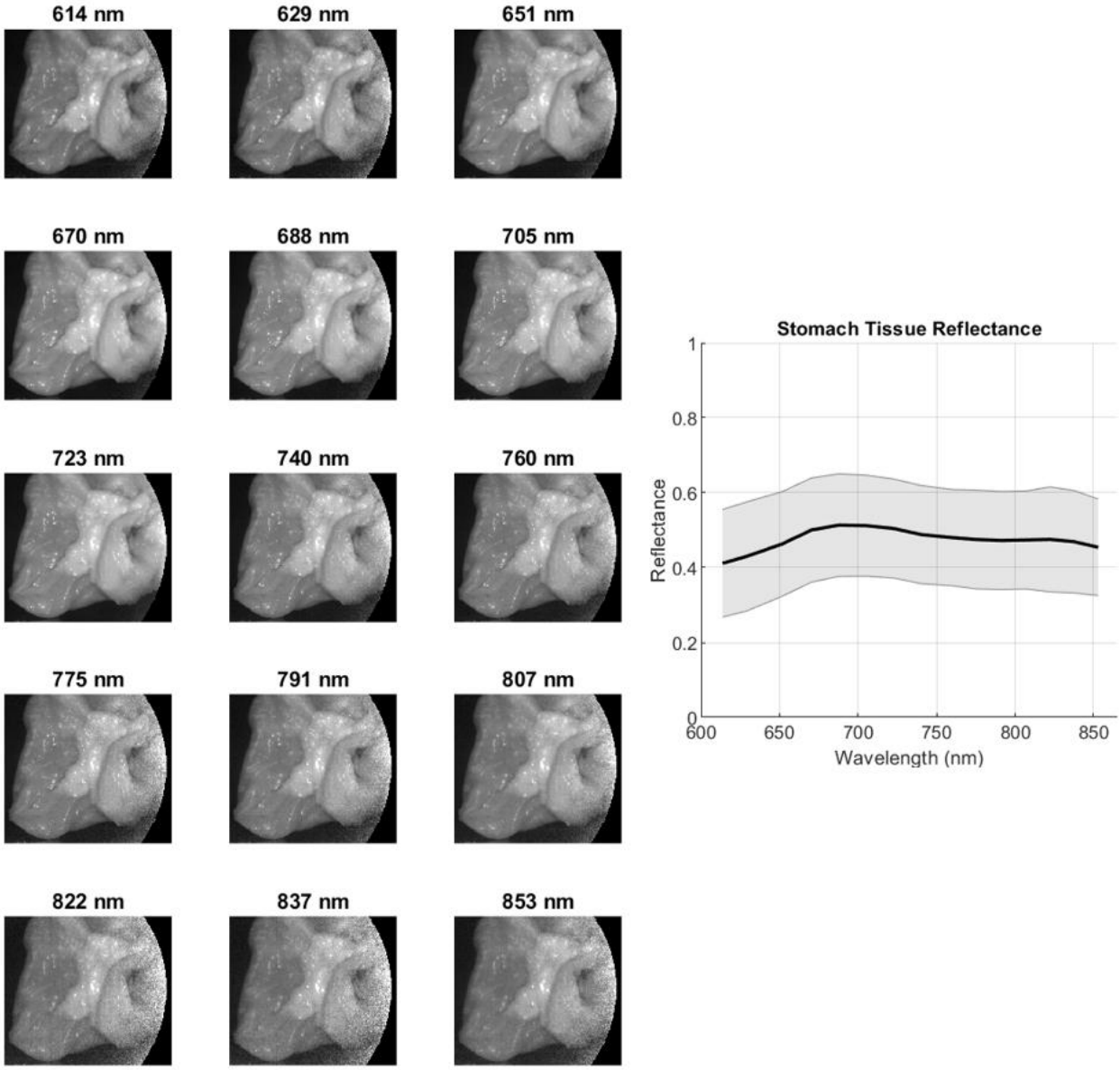

Figure 9. Hyperspectral image of porcine stomach tissue. Each band image is shown on the left, with the respective spectral curve on the right.

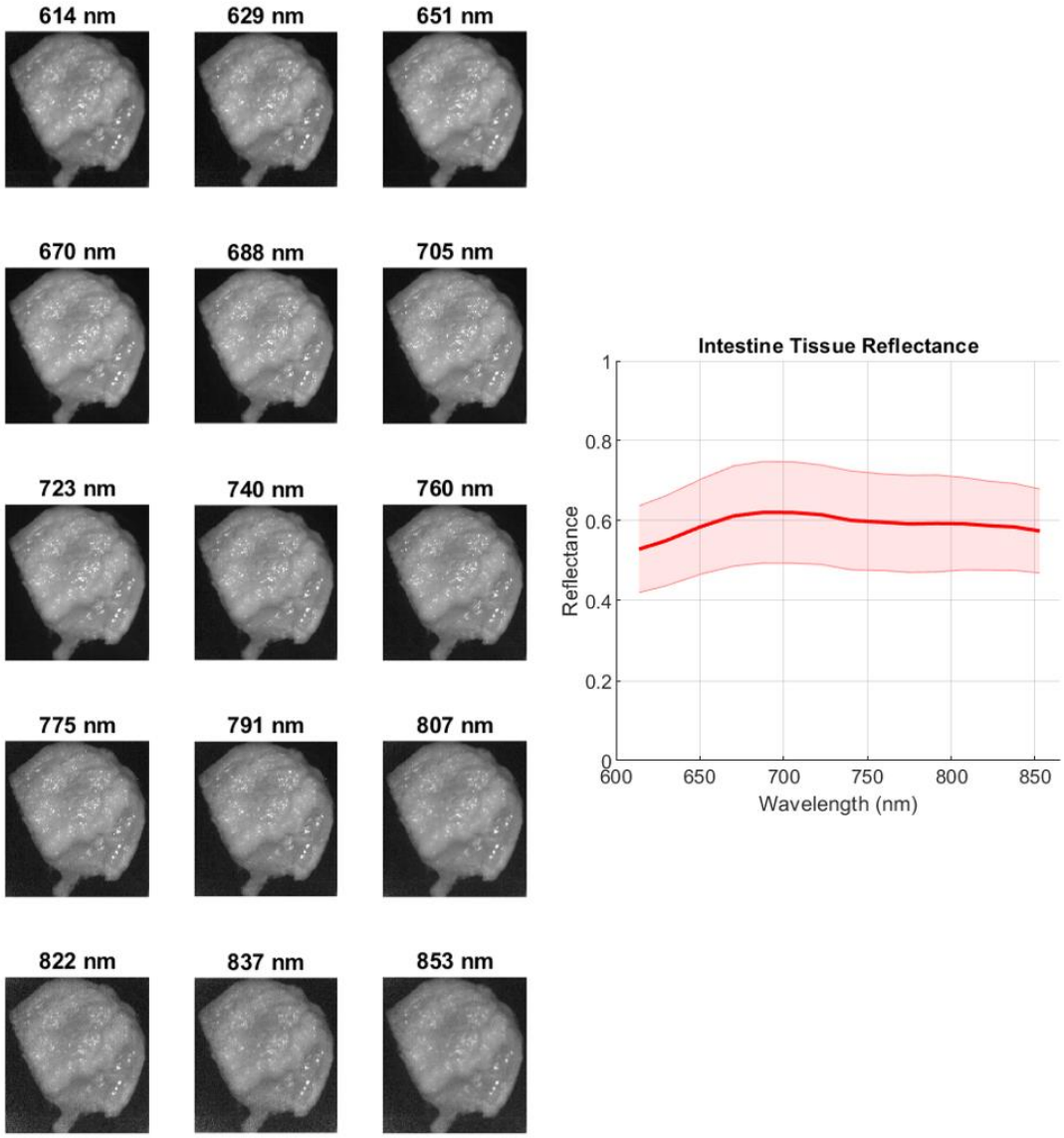

Figure 10. Hyperspectral image of porcine intestinal tissue. Each band image is shown on the left, with the respective spectral curve on the right.

4. DISCUSSION AND CONCLUSION

A high-speed hyperspectral system for laparoscopic imaging, capable of capturing a hypercube in approximately 0.1 s, paired with a processing framework, is shown and validated for clinical feasibility showing acceptable spatial and spectral resolution. *Ex-vivo* visceral tissues are imaged with the system to mimic tissues visualized during laparoscopic and robotic surgery and are analyzed according to their respective spectral footprints.

We developed and validated a high-speed hyperspectral laparoscopic imaging system for potential applications in image-guided surgery. Our system addresses the drawbacks of long acquisition times and bulkiness of current HSI systems. Through various imaging and processing techniques we show sufficient spatial resolution and spectral accuracy in a high-speed, lightweight HSI system for laparoscopy. To further test the capabilities of the system and simulate intracorporeal imaging, the system was used in a phantom procedure to visualize different abdominal tissues. The constructed system shows the ability to distinguish different visceral tissues based on their spectral reflectance patterns, a capability that will

be built upon in future studies. Future work will also explore the many applications of HSI as it relates to laparoscopic and robotic surgery and automated histopathological diagnosis, with an emphasis on different spectral ranges for various procedures. Preliminary work has been underway in utilizing multiple hyperspectral cameras with the laparoscopic system through a lens system and optical beam splitter. This will allow a wider spectral range to be achieved without switching cameras, and also provides an avenue to maintain high resolution RGB imaging in concert with hyperspectral imaging and processing.

ACKNOWLEDGMENTS

This research was supported in part by the U.S. National Institutes of Health (NIH) grants (R01CA156775, R01CA204254, R01HL140325, and R21CA231911), the Cancer Prevention and Research Institute of Texas (CPRIT) grant RP190588, and by an internal fund from the Department of Urology of UT Southwestern Medical Center.

REFERENCES

1. Rawla, P., *Epidemiology of Prostate Cancer.* World J Oncol, 2019. **10**(2): p. 63-89.
2. Alius, C., et al., *Indocyanine Green-Enhanced Colorectal Surgery—between Being Superfluous and Being a Game-Changer.* Diagnostics, 2020. **10**(10): p. 742.
3. Grosek, J. and A. Tomazic, *Key clinical applications for indocyanine green fluorescence imaging in minimally invasive colorectal surgery.* J Minim Access Surg, 2020. **16**(4): p. 308-314.
4. Baltussen, E.J.M., et al., *Hyperspectral imaging for tissue classification, a way toward smart laparoscopic colorectal surgery.* J Biomed Opt, 2019. **24**(1): p. 1-9.
5. Clancy, N.T., et al., *Intraoperative measurement of bowel oxygen saturation using a multispectral imaging laparoscope.* Biomedical Optics Express, 2015. **6**(10): p. 4179-4179.
6. Lu, G. and B. Fei, *Medical hyperspectral imaging: a review.* J Biomed Opt, 2014. **19**(1): p. 10901.
7. Köhler, H., et al., *Laparoscopic system for simultaneous high-resolution video and rapid hyperspectral imaging in the visible and near-infrared spectral range.* Journal of Biomedical Optics, 2020. **25**(08).
8. Pfahl, A., et al., *Video: Clinical evaluation of a laparoscopic hyperspectral imaging system.* Surg Endosc, 2022.
9. Ayala, L., et al., *Video-rate multispectral imaging in laparoscopic surgery: First-in-human application.* 2021.
10. Zhao, Z., et al., *Augmented reality technology in image-guided therapy: State-of-the-art review.* Proc Inst Mech Eng H, 2021. **235**(12): p. 1386-1398.
11. Zhang, X., et al., *A markerless automatic deformable registration framework for augmented reality navigation of laparoscopy partial nephrectomy.* International journal of computer assisted radiology and surgery, 2019. **14**(8): p. 1285-1294.
12. Zhang, W., et al., *Augmented Reality Navigation for Stereoscopic Laparoscopic Anatomical Hepatectomy of Primary Liver Cancer: Preliminary Experience.* Frontiers in Oncology, 2021. **11**: p. 996.
13. Yu, F., et al., *An augmented reality endoscope system for ureter position detection.* Journal of medical systems, 2018. **42**(8): p. 1-12.
14. Wakabayashi, T., et al., *Intraoperative perfusion assessment in enhanced reality using quantitative optical imaging: an experimental study in a pancreatic partial ischemia model.* Diagnostics, 2021. **11**(1): p. 93.
15. Urade, T., et al., *Hyperspectral enhanced reality (HYPER) for anatomical liver resection.* Surgical endoscopy, 2021. **35**(4): p. 1844-1850.
16. Tao, H.-S., et al., *Application of Real-Time Augmented Reality Laparoscopic Navigation in Splenectomy for Massive Splenomegaly.* World journal of surgery, 2021. **45**(7): p. 2108-2115.

17. Schneider, C., et al., *Comparison of manual and semi-automatic registration in augmented reality image-guided liver surgery: a clinical feasibility study.* Surgical endoscopy, 2020. **34**(10): p. 4702-4711.
18. Moccia, S., et al., *Uncertainty-aware organ classification for surgical data science applications in laparoscopy.* IEEE Transactions on Biomedical Engineering, 2018. **65**(11): p. 2649-2659.
19. Joeres, F., et al. *Audiovisual AR concepts for laparoscopic subsurface structure navigation*. in *Graphics Interface 2021*. 2021.
20. Jao, M.-L., et al., *Intracholecystic administration of indocyanine green for fluorescent cholangiography during laparoscopic cholecystectomy—A two-case report.* International journal of surgery case reports, 2020. **68**: p. 193-197.
21. Diana, M. *Fluorescence-based enhanced reality (FLER) for real-time estimation of bowel perfusion in minimally invasive surgery*. in *Molecular-Guided Surgery: Molecules, Devices, and Applications II*. 2016. International Society for Optics and Photonics.
22. Bernhardt, S., et al., *The status of augmented reality in laparoscopic surgery as of 2016.* Medical image analysis, 2017. **37**: p. 66-90.
23. Barberio, M., et al., *Quantitative fluorescence angiography versus hyperspectral imaging to assess bowel ischemia: A comparative study in enhanced reality.* Surgery, 2020. **168**(1): p. 178-184.
24. Najah, H., et al., *Specific computed virtual chromoendoscopy for detection of peritoneal carcinomatosis: an animal study.* Surgical endoscopy, 2017. **31**(10): p. 4034-4043.
25. Najah, H., et al., *A feasibility study of the use of computed virtual chromoendoscopy for laparoscopic evaluation of peritoneal metastases.* Surgical endoscopy, 2017. **31**(2): p. 743-751.
26. Lin, J., et al. *Probe-based rapid hybrid hyperspectral and tissue surface imaging aided by fully convolutional networks*. in *International Conference on Medical Image Computing and Computer-Assisted Intervention*. 2016. Springer.
27. Lin, J., et al., *Dual-modality endoscopic probe for tissue surface shape reconstruction and hyperspectral imaging enabled by deep neural networks.* Medical image analysis, 2018. **48**: p. 162-176.
28. Lin, J., et al. *Endoscopic depth measurement and super-spectral-resolution imaging*. in *International Conference on Medical Image Computing and Computer-Assisted Intervention*. 2017. Springer.
29. Leitner, R., et al., *Multi-spectral video endoscopy system for the detection of cancerous tissue.* Pattern Recognition Letters, 2013. **34**(1): p. 85-93.
30. Jones, G., et al. *Inference of tissue haemoglobin concentration from Stereo RGB*. in *International Conference on Medical Imaging and Augmented Reality*. 2016. Springer.
31. Clancy, N.T., et al., *Intraoperative colon perfusion assessment using multispectral imaging.* Biomedical Optics Express, 2021. **12**(12): p. 7556-7567.
32. Clancy, N.T., et al., *Multispectral imaging of organ viability during uterine transplantation surgery in rabbits and sheep.* Journal of Biomedical Optics, 2016. **21**(10): p. 106006.
33. Chalopin, C., et al., *Intraoperative Imaging for Procedures of the Gastrointestinal Tract*, in *Innovative Endoscopic and Surgical Technology in the GI Tract*. 2021, Springer. p. 365-379.
34. Barberio, M., et al., *HYPerspectral Enhanced Reality (HYPER): a physiology-based surgical guidance tool.* Surg Endosc, 2020. **34**(4): p. 1736-1744.
35. Baltussen, E.J.M., et al., *Hyperspectral imaging for tissue classification, a way toward smart laparoscopic colorectal surgery.* Journal of Biomedical Optics, 2019. **24**(01): p. 1-1.
36. Lau, L.W., et al., *Laparoscopic Liver Resection with Augmented Reality: A Preclinical Experience.* J Laparoendosc Adv Surg Tech A, 2019. **29**(1): p. 88-93.
37. Liu, X., et al., *Laparoscopic stereoscopic augmented reality: toward a clinically viable electromagnetic tracking solution.* J Med Imaging (Bellingham), 2016. **3**(4): p. 045001.
38. Penza, V., et al., *Context-Aware Augmented Reality for Laparoscopy.* 2018.

39. Bugby, S.L., J. Lees, and A. Perkins, *Hybrid intraoperative imaging techniques in radioguided surgery: present clinical applications and future outlook.* Clinical and translational imaging, 2017. **5**(4): p. 323-341.
40. Dell'Oglio, P., et al., *A DROP-IN gamma probe for robot-assisted radioguided surgery of lymph nodes during radical prostatectomy.* European Urology, 2021. **79**(1): p. 124-132.
41. Han, Y.B., et al., *SiPM-based gamma detector with a central GRIN lens for a visible/NIRF/gamma multi-modal laparoscope.* Optics Express, 2021. **29**(2): p. 2364-2364.
42. Kang, H.G., et al., *Proof-of-concept of a multimodal laparoscope for simultaneous NIR/gamma/visible imaging using wavelength division multiplexing.* Optics express, 2018. **26**(7): p. 8325-8339.
43. KleinJan, G., et al., *The best of both worlds: a hybrid approach for optimal pre-and intraoperative identification of sentinel lymph nodes.* European journal of nuclear medicine and molecular imaging, 2018. **45**(11): p. 1915-1925.
44. Kim, J.K., et al., *Multimodal imaging of laser speckle contrast imaging combined with mosaic filter-based hyperspectral imaging for precise surgical guidance*. IEEE Transactions on Biomedical Engineering, 2021.
45. Takamatsu, T., et al., *Over 1000 nm Near-Infrared Multispectral Imaging System for Laparoscopic In Vivo Imaging.* Sensors (Basel), 2021. **21**(8).
46. Jacques, S.L., *Corrigendum: Optical properties of biological tissues: a review.* Physics in Medicine and Biology, 2013. **58**(14): p. 5007-5008.